

Improved Reflection Models of Black-Hole Accretion Disks: Treating the Angular Distribution of X-rays

J. García

Harvard-Smithsonian Center for Astrophysics, 60 Garden St., Cambridge, MA 02138 USA

`javier@head.cfa.harvard.edu`

T. Dauser

Dr. Karl Remeis-Observatory and Erlangen Centre for Astroparticle Physics, Sternwartstr.

7, 96049 Bamberg, Germany

`thomas.dauser@sternwarte.uni-erlangen.de`

A. Lohfink

Department of Astronomy, University of Maryland, College Park, MD, USA & Joint
Space-Science Institute, University of Maryland, College Park, MD, USA

`alohfink@astro.umd.edu`

T. R. Kallman

NASA Goddard Space Flight Center, Greenbelt, MD 20771

`timothy.r.kallman@nasa.gov`

J. Steiner

Harvard-Smithsonian Center for Astrophysics, 60 Garden St., Cambridge, MA 02138 USA

`jsteiner@head.cfa.harvard.edu`

J. E. McClintock

Harvard-Smithsonian Center for Astrophysics, 60 Garden St., Cambridge, MA 02138 USA

– 2 –

`jem@cfa.harvard.edu`

L. Brenneman

Harvard-Smithsonian Center for Astrophysics, 60 Garden St., Cambridge, MA 02138 USA

`lbrenneman@cfa.harvard.edu`

J. Wilms

Dr. Karl Remeis-Observatory and Erlangen Centre for Astroparticle Physics, Sternwartstr.

7, 96049 Bamberg, Germany

`joern.wilms@sternwarte.uni-erlangen.de`

W. Eikmann

Dr. Karl Remeis-Observatory and Erlangen Centre for Astroparticle Physics, Sternwartstr.

7, 96049 Bamberg, Germany

`wiebke.eikmann@sternwarte.uni-erlangen.de`

C. S. Reynolds

Department of Astronomy, University of Maryland, College Park, MD, USA & Joint

Space-Science Institute, University of Maryland, College Park, MD, USA

`chris@astro.umd.edu`

F. Tombesi

Department of Astronomy, University of Maryland, College Park, MD, USA & X-ray
Astrophysics Laboratory, NASA Goddard Space Flight Center, Greenbelt, MD 20771, USA

`ftombesi@astro.umd.edu`

Received _____; accepted _____

ABSTRACT

X-ray reflection models are used to constrain the properties of the accretion disk, such as the degree of ionization of the gas and the elemental abundances. In combination with general relativistic ray tracing codes, additional parameters like the spin of the black hole and the inclination to the system can be determined. However, current reflection models used for such studies only provide angle-averaged solutions for the flux reflected at the surface of the disk. Moreover, the emission angle of the photons changes over the disk due to relativistic light bending. To overcome this simplification, we have constructed an angle-dependent reflection model with the `XILLVER` code and self-consistently connected it with the relativistic blurring code `RELLINE`. The new model, `relxill`, calculates the proper emission angle of the radiation at each point on the accretion disk, and then takes the corresponding reflection spectrum into account. We show that the reflected spectra from illuminated disks follow a limb-brightening law highly dependent on the ionization of disk and yet different from the commonly assumed form $I \propto \ln(1 + 1/\mu)$. A detailed comparison with the angle-averaged model is carried out in order to determine the bias in the parameters obtained by fitting a typical relativistic reflection spectrum. These simulations reveal that although the spin and inclination are mildly affected, the Fe abundance can be over-estimated by up to a factor of two when derived from angle-averaged models. The fit of the new model to the *Suzaku* observation of the Seyfert galaxy Ark 120 clearly shows a significant improvement in the constrain of the physical parameters, in particular by enhancing the accuracy in the inclination angle and the spin determinations.

1. Introduction

Despite the huge difference in mass, Galactic black holes (GBH) in binary systems and super-massive black holes in active galactic nuclei (AGN) show similar X-ray properties. In particular, in many sources an emission component is present, which is generated by high-energy coronal photons that are reprocessed in an optically-thick accretion disk. The most prominent feature in this component – commonly referred to as the “reflection” spectrum – is the Fe K emission line at 6–7 keV, which is produced by fluorescence. This reflection spectrum from the inner disk region carries information on the physical composition and condition of the matter in strong gravitational fields (e.g., Fabian et al. 2000; Fabian & Vaughan 2003; Reynolds & Nowak 2003; Dovčiak et al. 2004; Miller et al. 2008). Doppler effects, light bending and gravitational redshift skew the Fe line (and the fluorescence lines of other elements) and can, for rapidly spinning black holes, extend the red wing of the line to very low energies (Fabian et al. 1982; Laor 1991; Dabrowski et al. 1997; Dovčiak et al. 2004; Brenneman & Reynolds 2006; Dauser et al. 2010). Hence, in order to fit observations, the pure reflection spectrum has to be convolved by relativistic blurring algorithms that account for these relativistic effects (e.g., Miller et al. 2008; Steiner et al. 2011; Reynolds et al. 2012; Fabian et al. 2012a; Dauser et al. 2012). This relativistic smearing highly depends on the parameters of the system, like the black hole spin and the inclination of the system. However, most current reflection models used for such studies only provide an angle-averaged solution for the flux reflected at the surface of the disk, which can systematically affect the inferred disk parameters. Furthermore, an isotropic distribution or a particular limb-darkening law is often chosen (e.g. Chiang et al. 2012; Walton et al. 2013), despite the fact that radiative transfer calculations predict an emission excess near grazing angles (known as limb brightening, e.g., Róžańska & Madej 2008; Svoboda et al. 2009; Róžańska et al. 2011). In fact, the pioneer and widely used relativistic line convolution model `laor` (Laor 1991) intrinsically assumes a limb-darkening law.

Several authors have studied relativistic effects on the emission of X-rays from accretion disks, while considering the angular distribution of the radiation. Martocchia et al. (2000) performed calculations of the relativistic effects acting on both the reflection continuum and the iron line in a Kerr-metric, and they showed that for rapidly spinning black holes the line equivalent width is substantially enhanced. Reynolds et al. (2000) discussed (within the context the analysis of *ASCA* data for NGC 4258) how gravitational light bending can affect the Fe line emission in high-inclination sources. Beckwith & Done (2004) and Dovčiak et al. (2004) presented similar calculations emphasizing how the assumed angular emissivity law (limb darkening or brightening) can significantly affect the line profile when relativistic effects are important. These studies were extended by Niedźwiecki & Życki (2008) in order to explain the Fe line profile and variability observed in MCG–6-30-15. More recently, Svoboda et al. (2009) performed relativistic radiative transfer calculations of X-ray irradiated disk atmospheres with the NOAR code to determine the impact of light bending on X-rays in the 2–10 keV band. They concluded that the uncertainty in the angular distribution of reflected radiation can translate into a $\sim 20\%$ uncertainty in the determination of R_{in} , and thus also in the spin parameter a_* . The emphasis of their work is on the relativistic effects and the estimation of uncertainties, and they omit a detailed ionization-balance calculation of the reflection spectrum.

In the past, X-ray reflection from a cold, neutral slab for the K lines of heavy elements has been discussed extensively in the context of X-ray binaries (Basko 1978) and AGN (George & Fabian 1991; Matt et al. 1991). Additional earlier work treats the angular-dependence of electron scattering in cold material (Ghisellini et al. 1994), and in hot thermal plasmas (Haardt 1993), while neglecting photoelectric absorption and line emission. Matt et al. (1996) carried out detailed Monte Carlo calculations of the Fe $K\alpha$ emission from X-ray photoionized accretion disks, showing that the line strength and shape depend on both the ionization stage of the material and on the disk inclination

angle. Vrtilek et al. (1993) computed the disk corona structure in X-ray binaries under the assumptions of ionization, thermal, and hydrostatic balance of gas illuminated by the central continuum source. They explained the Fe K emission and the absorption edge in terms of the inclination angle and the shape of the incident source spectrum. More sophisticated ionized reflection calculations have been presented by Róžańska & Madej (2008) in the context of accretion disks around supermassive black holes; their models depict the effects of a limb-brightening law on the reflected X-rays. The reflection model that has been most widely used by observers, for both general application and for measuring black hole spin via the Fe-line method, is REFLIONX (Ross & Fabian 2005). This industry-standard model solves the radiation transfer problem using a diffusion equation, which imposes the limitation that the model can only deliver an angle-averaged spectrum.

We overcome the simplifications adopted by previous models – i.e., limited ionization balance calculations and angle-averaged reflected flux – by exploiting the full capabilities of our reflection code XILLVER (García & Kallman 2010; García et al. 2013), to treat the angular distribution of the reflected X-rays. The Feautrier method we employ (Feautrier 1964) enables XILLVER to calculate the specific intensity of the radiation field as a function of energy, position in the slab, and viewing angle. This allows us to construct a grid of reflection models in which the inclination angle is included as an explicit fitting parameter. Furthermore, using this approach we are able to address a further complication. Due to general relativistic light-bending, photons are emitted over a wide range of angles depending on their location on the accretion disk. This complication can be solved by directly linking the reflection code to a relativistic smearing kernel. Accordingly, we use the angle-dependent XILLVER reflection code to assign a proper reflected spectrum for each point on the disk, which then depends on the actual emission angle derived from general relativity. These single spectra are then relativistically smeared using RELLINE (Dauser et al. 2010, 2013) before being integrated to yield the total reflection spectrum. As each of

these emission points has to be treated separately, a simple combination of `XILLVER` and `RELLINE` will yield inconsistent results.

In this paper we present for the first time a complete description of the spectrum reflected by an ionized accretion disk around a black hole that is complete, self-consistent, and takes into account the angular distribution of the reflected X-rays. The new model, `relxill`, is provided in the standard format, enabling its use with commonly employed fitting packages such as `XSPEC` (Arnaud 1996) and `ISIS` (Houck & Denicola 2000); the model’s input parameters are the same as that of its parent model `relconv`. An additional version of the new model, `relxill_lp`, which simulates the reflected spectra assuming a lamppost geometry, is also supplied.

This paper is organized as follows: In Section 2, we describe our angle-dependent solution for the reflected spectrum and compare it with the commonly used angle-averaged solution. Sections 3 and 4 first explore how relativistic effects modify the reflected spectrum, and they then discuss how we integrated the reflection code `XILLVER` with the relativistic blurring code `RELLINE`. In Section 5, we assess, via a detailed error analysis, how the angle-averaged solution yields biased values of the various model parameters. An application of our model to an analysis of *Suzaku* data for Ark 120 is discussed in Section 6, and we offer our conclusions in Section 7.

2. Angular Solution of the Reflected Spectrum

The X-ray reflection calculations presented in this paper are based upon those from García et al. (2013), with the difference being that we now exploit the full capabilities of our reflection code `XILLVER` by extracting the solution of the emergent spectra for individual viewing angles. These models and the details of the numerical code have been extensively

described by García & Kallman (2010), García et al. (2011), and García et al. (2013). Here we will discuss the theoretical aspects concerning the angular dependence of the radiation fields, and their effects on the observed spectrum.

The basic layout of the reflection problem is shown in the diagram of Figure 1. The gas in the atmosphere of the accretion disk (i.e., within a few Thomson depths) is assumed to be at a density of $n_{\text{H}} = 10^{15} \text{ cm}^{-3}$, in a plane-parallel geometry, where the coordinate of importance is shown in the vertical direction perpendicular to the slab (z -axis). The surface of the disk is set at $\tau_{\text{T}} = 0$, and the base of the atmosphere at $\tau_{\text{max}} = 10$, where $d\tau_{\text{T}} = 1.2n_{\text{H}}\sigma_{\text{T}}dz$ is the Thomson optical depth, and $\sigma_{\text{T}} = 6.65 \times 10^{-25} \text{ cm}^2$ is the Thomson classical cross section for electron scattering.

The disk is illuminated by a primary source of X-ray radiation from above. The radiation enters the slab at $\tau_{\text{T}} = 0$, and is reprocessed by the atmosphere. The intensity of the radiation field $I(z, \mu, \varepsilon)$ at each position z the atmosphere, per energy ε , unit area, and steradian is determined by solving the time-independent, one-dimensional plane-parallel radiation transfer equation

$$\mu \frac{\partial I_{\varepsilon}(z, \mu)}{\partial z} = \eta_{\varepsilon}(z) - \chi_{\varepsilon}(z)I_{\varepsilon}(z, \mu) \quad (1)$$

where μ is the cosine of the angle θ with respect to the disk normal, and $\eta_{\varepsilon}(z)$ and $\chi_{\varepsilon}(z)$ are the total emissivity and opacity, respectively.

At each point in the slab one can distinguish between the incoming and the outgoing components of the radiation for $\pm\mu$ (see Figure 1), and thus write two separate transfer equations

$$\mu \frac{\partial I_{\varepsilon}^{+}(\tau_{\varepsilon}, \mu)}{\partial \tau_{\varepsilon}} = I_{\varepsilon}^{+}(\tau_{\varepsilon}, \mu) - S_{\varepsilon}(\tau_{\varepsilon}) \quad (2)$$

$$-\mu \frac{\partial I_{\varepsilon}^{-}(\tau_{\varepsilon}, \mu)}{\partial \tau_{\varepsilon}} = I_{\varepsilon}^{-}(\tau_{\varepsilon}, \mu) - S_{\varepsilon}(\tau_{\varepsilon}) \quad (3)$$

where I_{ε}^{+} and I_{ε}^{-} refer to positive and negative values of μ , respectively, and $\tau_{\varepsilon} = -\chi_{\varepsilon}(z)dz$

is the total optical depth. By defining the symmetric and anti-symmetric averages

$$u_\varepsilon(\tau_\varepsilon, \mu) = \frac{1}{2} [I_\varepsilon^+(\tau_\varepsilon, \mu) + I_\varepsilon^-(\tau_\varepsilon, \mu)] \quad (4)$$

$$v_\varepsilon(\tau_\varepsilon, \mu) = \frac{1}{2} [I_\varepsilon^+(\tau_\varepsilon, \mu) - I_\varepsilon^-(\tau_\varepsilon, \mu)] \quad (5)$$

the transfer equation (1) can be rewritten as

$$\mu^2 \frac{\partial^2 u_\varepsilon(\tau_\varepsilon, \mu)}{\partial \tau_\varepsilon^2} = u_\varepsilon(\tau_\varepsilon, \mu) - S_\varepsilon(\tau_\varepsilon), \quad (6)$$

where $S_\varepsilon(\tau_\varepsilon) = \eta_\varepsilon/\chi_\varepsilon$ is the source function. The line plus continuum emissivities and opacities depend on the structure of the gas, which is determined at each point in the slab by the photoionization code XSTAR (Kallman & Bautista 2001). Details on the calculation of these quantities and on the atomic data implemented in these calculations are fully described in García & Kallman (2010) and García et al. (2013). Expression (6) is a second-order differential equation subject to two boundary conditions. At the top ($\tau_\varepsilon = 0$), the incoming radiation field $I_\varepsilon^-(0, \mu)$ is known. Since $u_\varepsilon - v_\varepsilon = I_\varepsilon^-$, and $v_\varepsilon = \mu \frac{\partial u_\varepsilon}{\partial \tau_\varepsilon}$, the boundary condition at the surface of the slab can be expressed as

$$u_\varepsilon(0, \mu) - \mu \left(\frac{\partial u_\varepsilon}{\partial \tau_\varepsilon} \right)_0 = I_{\text{inc}}. \quad (7)$$

Assuming no irradiation from below, we set $I_\varepsilon^+(\tau_{\text{max}}, \mu) = 0$ at the bottom of the atmosphere ($\tau_\varepsilon = \tau_{\text{max}}$). Thus, using $u_\varepsilon + v_\varepsilon = I_\varepsilon^+$, the boundary condition at the bottom of the slab becomes

$$u_\varepsilon(\tau_{\text{max}}, \mu) + \mu \left(\frac{\partial u_\varepsilon}{\partial \tau_\varepsilon} \right)_{\tau_{\text{max}}} = 0 \quad (8)$$

and $\tau_{\text{max}} = 10\tau_{\text{T}}$ is chosen for all the calculations.

The transfer equation (6) and its boundary conditions (7) and (8) are converted into a set of difference equations via the discretization of all variables, in the form

$$\mu^2 u_i'' = u_i - S_i \quad (9)$$

where $i = 1, \dots, N$ denotes a particular position in a grid of N points τ_i . Notice that, for simplicity, we have intentionally suppressed the explicit dependence on ε and μ .

The derivatives of u_i in a non-uniform mesh can be found using the Taylor's expansions

$$u_{i+1} = u_i + u'_i \Delta\tau_i + u''_i \frac{\Delta\tau_i^2}{2} + \dots \quad (10)$$

$$u_{i-1} = u_i - u'_i \Delta\tau_{i-1} + u''_i \frac{\Delta\tau_{i-1}^2}{2} + \dots \quad (11)$$

which are usually referred to as the forward and backward finite differences. Solving for u'_i in (10) and substituting in (11), the second derivative can be expressed as

$$u''_i = \frac{2}{\Delta\tau_i + \Delta\tau_{i-1}} \left[u_{i-1} \left(\frac{1}{\Delta\tau_{i-1}} \right) - u_i \left(\frac{\Delta\tau_i + \Delta\tau_{i-1}}{\Delta\tau_i \Delta\tau_{i-1}} \right) u_{i+1} \left(\frac{1}{\Delta\tau_i} \right) \right]. \quad (12)$$

This can now be inserted into (9) to write

$$u_{i-1} \left[\frac{-2\mu^2}{\Delta\tau_{i-1}(\Delta\tau_i + \Delta\tau_{i-1})} \right] + u_i \left[\frac{2\mu^2}{\Delta\tau_i \Delta\tau_{i-1}} \right] + u_{i+1} \left[\frac{-2\mu^2}{\Delta\tau_i(\Delta\tau_i + \Delta\tau_{i-1})} \right] = S_i \quad (13)$$

Equation (12) can be inserted into (10) to get a similar expression for the first derivative in terms of u_{i-1} , u_i , and u_{i+1} . However, for the boundary condition at the top

$$u_1 - \mu u'_1 = I_{\text{inc}} \quad (14)$$

a different expression is needed. An alternative is to rely upon the second derivative provided by equation (9). Thus

$$u'_i = u_{i+1} \left(\frac{1}{\Delta\tau_i} \right) - u_i \left(\frac{1}{\Delta\tau_i} + \frac{\Delta\tau_i}{2\mu^2} \right) + S_i \frac{\Delta\tau_i}{2\mu^2} \quad (15)$$

and (14) becomes

$$u_1 \left(1 + \frac{\mu}{\Delta\tau_1} + \frac{\Delta\tau_1}{2\mu} \right) - u_2 \left(\frac{\mu}{\Delta\tau_1} \right) = I_{\text{inc}} + S_1 \frac{\Delta\tau_1}{2\mu} \quad (16)$$

A similar expression can be found for the inner boundary at $\tau = \tau_{\text{max}}$.

The numerical solution in this approach proceeds by a forward elimination plus backward substitution scheme. We start using the boundary condition at the surface to express u_1 in terms of u_2 . The result is then applied to variables u_1 , u_2 and u_3 in order to express u_2 in terms of u_3 . Iteratively, and in the same way, we can express each u_i in terms of u_{i+1} . We finally reach the last point in the grid, and the boundary condition for τ_{\max} gives u_N . Back substitutions then produce $u_N \rightarrow u_{N-1} \rightarrow u_{N-2} \rightarrow \dots \rightarrow u_2 \rightarrow u_1$, so all u_i are known.

Once the solution for all u_i is known, it is trivial to obtain the outgoing intensity $I^+(0)$ at the surface of the slab (the reflected component), by simply using (4)

$$I_1^+ = 2u_1 - I_1^- \quad (17)$$

where, again, $I_1^- = I_{\text{inc}}$. This is the solution of the reflected intensity at the illuminated surface of the slab for every energy E and every angle μ . For the calculations presented here, the grid in μ angles is defined as

$$\mu_j = \frac{j - 0.5}{M} \quad (j = 1, 2, \dots, M) \quad (18)$$

with $M = 10$, and $\Delta\mu = 1/M$. Note that for the XILLVER models previously published (García & Kallman 2010; García et al. 2011, 2013), the reflected spectra were provided in terms of the *angle-averaged* quantity,

$$F_\epsilon^+(0) = \frac{1}{2} \int_0^1 I_\epsilon^+(0, \mu) \mu d\mu \quad (19)$$

defined as the first moment of the radiation field (although we are only taking the component of the field for positives μ , the one that reaches the observer).

The left column in Figure 2 shows the reflection spectra across all viewing angles for different values of the ionization parameter, as indicated in each panel. These are displayed in different colors (see right column for an identification). At first glance the spectra look

very similar to each other. However, the ratio between spectra for individual μ and the angle-averaged spectrum reveals differences that can reach up to a factor 2.5. Especially interesting is that the spectral features behave differently than the continuum. This makes sense because the viewing angle affects the intensity of the emergent radiation by changing the *effective optical depth*, given by the geometrical projection of the optical depth along the line of sight according to

$$\tau_{\text{eff}} = \tau / \mu \quad . \quad (20)$$

An observer looking at grazing angles (small μ) will effectively see a larger optical depth. Or in other words, photons emitted at a particular depth in the slab will see a larger effective depth to escape out of the disk at grazing angles. Therefore, looking at the energy distribution of the emergent radiation, spectral features that are originally produced at large τ (such as those from Fe and Ni) will be more attenuated than those that are produced near the surface (such as C, N, and O lines). This is also the case for photons in the continuum, which is the reason for the Compton hump above 20 keV being strongly affected by the viewing angle (Lightman & Rybicki 1980; Lightman et al. 1981; Lightman & White 1988; Magdziarz & Zdziarski 1995). In fact, high energy photons are the most affected, since they experience a larger number of scatterings (thus, they will be very sensitive to any small change in the optical depth).

The angular dependence of the reflected spectra for energies above ~ 20 keV is the same for all ionization parameters, since Compton scattering is the main source of opacity, and these energies are insensitive to the gas temperature. Conversely, the impact of the viewing angle at lower energies is more pronounced where the photoelectric opacity becomes important. Because low-ionization models are dominated by photoelectric absorption, angular effects are accordingly stronger the lower the ionization parameter. An important effect is the change in the slope of the reflected spectrum, as the angular dependence of the solution is different at different energies. In general, models with an inclination of

60°-70° seem to be the closest to the angle-averaged solution. Therefore, we expect the models presented here to be most useful for systems with either very low or very high inclination angles.

The energy dependence of the angular effects on the reflected spectrum becomes very relevant when combined with relativistic blurring models, such as `RELLINE`. Commonly, in these models one can choose between a limb-brightening or a limb-darkening law which behaves uniformly for all energies (Svoboda et al. 2009; Dauser et al. 2010, 2013). In the right column of Figure 2, we compare the intensity predicted by our angular dependent simulation with these empirical models. It is clear that our simulations tend towards limb brightening, i.e., the integrated flux increases when the inclination angle increases. For low ionization models, the predicted trend departs significantly from the usual limb-brightening law, showing a much flatter profile. As the ionization grows, the integrated flux predicted by `XILLVER` becomes steeper and approaches the limb-brightening law. However, for $\log \xi \gtrsim 3$, the profile becomes flatter, resembling isotropic behavior. This is due to the fact that for high-ionization models, the ionization structure is dominated by electron scattering, rather than photoionization and recombination. In this regime, photons suffer a large number of scatterings in a hot atmosphere before escaping towards the observer. The gas remains close to the Compton temperature for a large range of optical depths (García et al. 2013), meaning that an observer will see a nearly isothermal atmosphere at any inclination. These results are of great relevance when contrasted with earlier relativistic convolution models (e.g., `kdblur`, `kerrconv`), which arbitrarily assume a limb-darkening law (Laor 1991). Instead, all our models predict a limb-brightening behavior highly dependent on the particular ionization state of the gas.

We have also explored the possibility of including an angular dependence in the scattering term of the source function of Equation (9). In the absence of absorption

and intrinsic emission (i.e., pure scattering), the source function is simply reduced to $S_\varepsilon(\tau_\varepsilon) = J_\varepsilon(\tau_\varepsilon)$, where $J_\varepsilon(\tau_\varepsilon) = \int u_\varepsilon(\mu, \tau_\varepsilon) d\mu$ is the zeroth moment of the radiation field (i.e., the mean intensity), which is an angle-averaged quantity. One can, however, introduce a phase function to describe the angular properties of the electron scattering. A simple approximation in the non-relativistic limit is the Rayleigh scattering phase function, for which the source function can be expressed as

$$S_\varepsilon(\tau_\varepsilon, \mu) = \frac{3}{8}[(3 - \mu^2)J_\varepsilon(\tau_\varepsilon) + (3\mu^2 - 1)K_\varepsilon(\tau_\varepsilon)] \quad (21)$$

(see Eq. 103, Chap. 1 of Chandrasekhar 1960), where $K_\varepsilon(\tau_\varepsilon) = \int u_\varepsilon(\mu, \tau_\varepsilon) \mu^2 d\mu$ is the second moment of the radiation field. Using this form of the source function we have calculated the radiation transfer on an isothermal, pure scattering atmosphere. Figure 3 shows that the angular distribution of the integrated flux behaves very closely to the isotropic case. This result demonstrates that the treatment of the Compton scattering in XILLVER is adequate for these kind of calculations and it is upheld by 3-dimensional Monte Carlo simulations which have shown that the reflection intensity of a Compton scattering dominated atmosphere appears nearly isotropic for all viewing angles.

3. Accretion Disks in General Relativity

In this section we discuss the effects of strong gravity on photons emitted from the surface of an accretion disk around compact objects, and the numerical methods employed to predict the emitted spectrum perceived by a distant observer. In the following we briefly summarize how we calculate the general relativistic radiative transfer around a rotating black hole. Accordingly, the equations of motion in the Kerr (1963) metric are used to describe the photon and particle trajectories (Bardeen et al. 1972). The actual transfer is solved by using “Cunningham Transfer Function” (Cunningham 1975), as implemented by Speith et al. (1995). This approach is used by the RELLINE code, which was employed to

obtain the results presented in the following.¹

In the following, we use the dimensionless spin parameter a_* , which takes values from $a_* = 1$ (maximally rotating) to $a_* = 0$ (non-spinning) and $a_* = -1$ (negatively rotating, i.e., the black hole and the accretion disk are counter rotating). Moreover, all lengths are given in units of the gravitational radius, which is defined as $r_g = GM/c^2$.

Using the approach outlined above, we are able to calculate the apparent image of the accretion disk on the sky a distant observer would see (e.g. Cunningham & Bardeen 1973). Figure 4 shows how light-bending creates apparent asymmetries in the shape and warps the disk towards the observer. Moreover, the energy shift the photons experience from the disk to the observer is illustrated as it varies over the disk (see Dauser et al. 2010, for more details and explicit formulae). The main effects which impact the energy are the Doppler shift (which leads to the blue and red division of the disk) and the gravitational redshift, which increases with proximity to the black hole.

Besides the energy shift, general relativistic effects also alter the direction of the photon, i.e., the photon is likely to be emitted at a different angle than it is observed. From the momentum of the emitted photon \vec{p}_e (see Bardeen et al. 1972), the emission angle can be easily calculated via

$$\cos(\theta_e) = \frac{\vec{p}_{e\perp}}{|\vec{p}_e|} \quad . \quad (22)$$

Figure 5 shows a map of θ_e on the surface of a disk seen at inclinations of $\theta = 40^\circ$ and $\theta = 80^\circ$. In both cases, the emission angle converges as expected towards the viewing angle θ at sufficiently large distances from the central black hole. This is expected, as this implies that the photon travels on a straight trajectory to the observer. In particular for $\theta = 40^\circ$, slight differences at larger distances are visible between the left and the right sides, due to

¹See Dauser et al. (2010, 2013) for more details on the calculation and the code.

the rotation of the accretion disk. Looking at the zoomed images in Figure 5, it is obvious that essentially every emission angle from 0° and 90° provides some contribution to the observed image. Specifically, θ_e is significantly lower than the viewing angle for photons emitted behind the black hole, as light bending effects are stronger in this case. Even for $\theta = 80^\circ$, the emission angle approaches 0° for a small part of the disk. Again, due to the rotation of the disk and also the rotation of the black hole, this effect is stronger for particles moving towards the observer and in the rotational direction of the black hole. Therefore, the region of low emission angles is in both cases shifted asymmetrically to the left. Additionally, there is also a region of relatively high emission angles at the innermost radii of the disk. This is best seen for $\theta = 40^\circ$, visible as a blue ring in Figure 5. Note that although most of the emission angles in the figure are close to the viewing angle, the inner parts radiate with much stronger intensity and generally dominate the observation. In detail, for a standard Shakura & Sunyaev (1973) disk the emitted intensity behaves like $I \propto r^{-3}$, while for a disk irradiated by a source on the black hole’s rotational axis, generally, an even steeper profile is expected (e.g., Fukumura & Kazanas 2007; Wilkins & Fabian 2012; Dauser et al. 2013).

4. Angle-Dependent Blurred Reflection

As discussed in Section 2, the reflection spectra change significantly depending on the inclination angle. Moreover, in the previous section we showed that the emission angles are not necessarily equal (or even close) to the inclination angle of the system. Therefore, it is imperative to take into account the complete relativistic transfer function for each region on the accretion disk, in order to properly predict the emitted spectrum.

4.1. General Properties (`relxill`)

For this purpose, we have extended the relativistic blurring code `RELLINE` and incorporated angle-dependent reflection from the `XILLVER` code. Accordingly, the model behaves similarly to a convolution of the `xillver` tables with `relconv`. But instead of smearing the angle averaged reflection, this new model, called `relxill`, combines the spectra from all points in the image plane according to their observed emission angles, all while properly smearing each point relativistically. Although more physically rigorous, under this new approach, no additional parameters enter the model. In fact, because the angular solution of the reflected spectrum is self-consistently calculated, no assumptions have to be made for the limb-brightening/darkening laws, and thus the `limb` parameter is removed from the model. However, we have included a flag variable called `angleon` to switch between the new model with the full angular solution (`angleon=1`), and the old angle-average version (`angleon=0`). This model is provided in the appropriate format to be used in combination with other models included in the commonly-used X-ray fitting packages such as `XSPEC` (Arnaud 1996) and `ISIS` (Houck & Denicola 2000).

It is important to clarify that a simple convolution of the angle-dependent `xillver` spectra with a relativistic blurring code will yield incorrect results. As described in Section 3, in presence of relativistic effects photons emitted at many different angles can contribute to the spectrum observed at one particular inclination, due to strong light-bending. This effect is different at different locations on the surface of the accretion disk. Therefore, the convolution of the reflected spectra needs to be done differently at each particular radius, taking the correct contribution of the multiple angular solutions to the given viewing angle. Figure 6 illustrates the differences in the final spectrum obtained from an simple convolution of `relconv` on the angle-dependent `xillver` spectra with the inclination angles linked together, and the one calculated self-consistently with our new

model `relxill`.

In Figure 7 we show the results of the new model `relxill` with typical parameter settings for different inclinations of the system. As is well known and evident in the spectra in the left panel, different inclinations primarily result in a net energy shift for the spectrum. However, when compared to the usual, averaged relativistic convolution (middle panel) it is obvious that a deviation is present which is highly dependent on the inclination. In general, these deviations are as large as 20% and distinct for lines and for the continuum. The reason for such differences becomes evident in the right panel, which shows the distribution of the flux per emission angle. In this particular case, there is a flat distribution at large inclinations ($\theta = 80^\circ$), i.e., photons from almost all angles are being observed with a similar contribution. Consequently, the resulting spectra are also very similar. This is equivalent to an angle-averaged solution, which is assumed by common reflection codes. In contrast, for small inclination angles the distribution is peaked at the actual inclination angle. This leads to an intrinsically different reflection spectrum and hence the relativistically smeared spectrum also differs significantly. However, these results depend upon various parameter settings, like the ionization of the disk (ξ), the abundances, the photon index Γ , the emissivity ϵ , or the spin a_* .

Note that while for low spin the relativistic effects are generally less pronounced, this does not mean that the difference between the average and the proper angle treatment vanishes. As it can be seen in Figure 2, even in the non-relativistic case, the averaged spectrum coincides best with the spectrum emitted at $\theta = 65^\circ$ and usually differs in shape for other smaller and larger inclinations.

4.2. Differences to the Angle-Average (`relxill_lp`)

Recent measurements (Wilms et al. 2001; Fabian et al. 2002; Brenneman & Reynolds 2006; Dauser et al. 2012; Fabian et al. 2012b; Gallo et al. 2011; Ponti et al. 2010; Brenneman et al. 2011, 2013; Duro et al. 2011; Miller et al. 2006; Reis et al. 2008) have revealed a steeper emissivity at the inner parts of the accretion disk than the canonically assumed r^{-3} dependence (Shakura & Sunyaev 1973). This is well understood in the so-called “lampost” geometry (Matt et al. 1991; Martocchia & Matt 1996). For this scenario, instead of coming from a corona around the inner regions of the disk (Haardt 1993; Dove et al. 1997), the primary radiation illuminating the disk comes from a source placed on the rotational axis of the black hole (e.g., Dauser et al. 2013, for a detailed discussion). Recent analyzes show that this model is capable of explaining the observed spectra in some systems (e.g., Wilkins & Fabian 2011; Duro et al. 2011; Dauser et al. 2012).

Due to the success of this model, we investigate the effect of a rigorous and full treatment of the emission angle on the parameters describing the reflection and the relativistic blurring. Under lampost geometry, the emissivity profile is specified by the height h of the primary source. While a large height usually implies a flat emissivity in the inner region, it steepens dramatically for decreasing height (e.g., Dauser et al. 2013). This means that for a source located near the black hole (low h), the inner portion of the accretion disk more strongly dominates the reflection spectrum than for a source located far away (high h).

Figure 8 shows the result of incorporating the angle-dependent reflection models from XILLVER into lampost geometry, synthesized with the relativistic blurring code into the end-product `relxill_lp` (Dauser et al. 2013). Each row represents a different inclination angle of the system (as indicated in the left panels). In all of the panels, each color represent a different height of the illumination source (as indicated in the middle panels).

The left column shows the integrated spectra reflected from the disk over all considered heights of the source. Intuitively and evidently, the closer the proximity of the source to the black hole, the stronger the relativistic effects that distort the shape of the lines. The middle column contains the ratio of each spectrum to the solution predicted using the angle-averaged case. Significant differences can be seen across the entire energy spectrum. For both very low and very high inclinations, the discrepancies in the Fe K line region can be as large as 40%. As expected, the differences with respect to the angle-averaged solution are smaller for intermediate inclinations. The right column shows the distribution of emission angles for each configuration. In other words, these panels show the relative contribution of photons emitted from different angles to a spectrum corresponding to an observation at a particular inclination. As expected, the distribution peaks at the viewing angle, in particular when the source is located far away from the center. For cases where the height of the illumination source is low ($h \sim 2 - 10 r_g$), the distribution can become very flat, and even more so when the disk is observed at large inclination angles. A very similar result can be seen for the models with $\log \xi = 3$ (Figure 8, middle column). Notice that when the distribution of the emission angle becomes very flat, the resultant spectrum is very similar to the angle-averaged solution (since in this case the observer is detecting photons coming from all angles with similar contributions, which has the effect of averaging the signal).

An important caveat to notice is that all the XILLVER models have been calculated implementing an incident irradiation at 45° with respect to the disk normal. As discussed in García & Kallman (2010) and Dauser et al. (2013), the incidence angle affects the specific intensity at the illuminated boundary of the slab, which influences to certain degree its ionization structure. The assumption is that the differences introduced by the incidence angle can be mimicked by a change in the ionization parameter. However, in the context of a lampost scenario these effects could have a larger impact on the simulated spectrum. A

proper treatment of variable incidence angles requires a much larger calculation of reflection models which is beyond the scope of the present work, but it will be implemented in future versions of the model.

5. Estimating Bias from Angle-Averaged Reflection Results

As evident from the previous section, significant differences exist when using the angle-averaged emissivity instead of the proper relativistically lensed treatment. However, prior to this work, the only available models for data fitting were angle averaged. Hence, we aim to determine to what extent this approximate treatment affects the fitted parameters as well as what can be gained by using the fully relativistic emissivity angle distribution.

In order to estimate the degree of bias from a typical observation, we produce a spectrum of an AGN showing relativistic reflection by simulating a 100 ksec observation with *XMM-Newton* assuming an unblurred reflection component with flux comparable to MCG–6-30-15 (Brenneman & Reynolds 2006). We employ the lampost version of our new model (`relxill_lp`) for the intrinsic, emitted reflection from which the observation is obtained. Subsequently, the simulated data is then fit by a commensurate (and common) angle-averaged model for X-ray reflection, by setting the flag `angleon=0`².

Figure 9 shows the bias estimates obtained from the simulation. In general, the behavior of the fitting parameters can be divided into two classes, depending on the irradiation of the accretion disk. These classes are delineated by the emissivity profile as (a): showing strong, centrally-concentrated emissivity which predominantly fluoresces the innermost accretion disk (a high inner emissivity index), and (b): showing a flattened

²Note that setting `angleon=0` is equivalent to implement a relativistically blurred reflection in the common fashion such as `relconv_lp` \times `xillver`

emissivity profile with a scaling below r^{-3} . Class (a) is readily understood as resulting from a low source height, whereas (b) represents a larger source height which provides a more uniform illumination of the inner disk. In the following we will interpret these results in detail. The values of our bias estimates, for both classes, can be found in Table 1.

In order to study class (a) in which the emissivity is steep (Figure 9, left panels), we use a source height of $h = 3r_g$. In general, it is evident that the iron abundance is most affected. In almost all the simulations the abundance is over-predicted and generally the effect is largest for low inclination angles. For a large spin ($a_* = 0.99$) and an almost neutral disk ($\xi = 1$), this effect can be more than a factor of two. For high inclinations this effect is reduced for all parameter configurations, while for $a_* = 0.0$ and $\xi = 1$ this turns into the opposite trend. Especially interesting is how the angle-averaged treatment influences spin determination. For the usual AGN observation (large spin, low ionization disk) there seem to be only very slight deviation from the input parameters. If the ionization is larger ($\xi = 10^3$), then stronger biases arise: A large spin ($a_* = 0.99$) will lead to an underestimate when fitting with angle-averaged models for low inclinations ($\theta < 50^\circ$), while for larger inclinations ($\theta > 60^\circ$), low spin values ($a_* = 0.0$) can be overestimated (but with large uncertainties). The inclination itself is essentially unaffected by the angle-averaged treatment. Only in the case of very low inclinations ($\theta < 40^\circ$) and high spin, the inferred inclination can be slightly overestimated (low ionization) or underestimated (high ionization), but the change is still quite small.

In the other instance (class b), Figure 9 (right panels) shows the results for a primary irradiating X-ray source placed at $h = 50r_g$. For this particular choice of parameters the spin cannot be very well constrained (see Dauser et al. 2013), and thus we analyze the effect of the averaged-angle treatment on the fitted height of the primary source, which is equivalent to determining the steepness of the emissivity profile. As in class (a), iron

abundance is generally overestimated. However, the absolute bias is only around 20% which is much lower for (b) compared to the bias obtained from the steep emissivity of (a). As before, this effect diminishes for higher inclinations. For the fitted inclination and the fitted height of the primary source, the degree of bias is very similar: A significant difference is only obtained for large inclinations ($\theta > 60^\circ$), in the sense that at increasing values of (input) inclination, the determination of height and the inclination will be underestimated by angle-averaged models. This effect is again much stronger and more significant for a low ionization of the accretion disk.

6. Application to Observational Data

To illustrate how the discussed changes in the model influence the spectroscopic results of a real dataset, we study the *Suzaku* spectrum of the ‘bare’ Seyfert 1 galaxy Ark 120. The term ‘bare’ refers to the weak amount of any intrinsic absorption, which simplifies the spectral analysis considerably (Patrick et al. 2011). The ~ 100 ks exposure (ObsID:702014010) was taken in April 2007 and reduced following the instructions of the *Suzaku* ABC Guide using the newest available calibration. For the spectral analysis, the two front-illuminated CCDs were co-added and binned to a signal-to-noise of 10. The energies 0.7 – 10 keV were noticed for fitting. The PIN data was used from 15 – 45 keV and binned to a signal-to-noise of 5. The back-illuminated XIS chip (XIS1) was not considered for this analysis. Nardini et al. (2011) and Walton et al. (2013) already showed that the spectrum of Ark 120 can be well described by a simple reflection model, including both a cold and blurred ionized reflector. Utilizing a similar model set-up to Walton et al. (2013), as well as applying the same restrictions to the parameters, we first describe the spectrum with the angle-averaged version of our new model `relxill` (by setting the flag `angleon=0`) for the blurred ionized reflector, and the cold reflector with a simple `XILLVER` table (with ξ

fixed to 1). The key parameters of this fit are presented in Table 7. In particular, we derive a spin of $a_* = 0.674_{-0.203}^{+0.118}$ and an inclination of $i = 45.0_{-2.7}^{+5.3}$ deg. To see the influence of the angle-dependence we then set the flag **angleon=1** for the blurred reflector, and replace the cold reflector with the angle dependent version of the XILLVER table. The inclination angles of the two reflectors were linked for fitting. Similar to the angle-averaged fit the quality is very good and the spectrum is well described by this model (see Figure 10). The angle-dependence improves the spin constraint to $a_* = 0.655_{-0.126}^{+0.122}$ and also improves the constraint on the inclination slightly ($i = 45.3_{-2.4}^{+4.8}$ deg). This is in agreement with the difference from the angle-averaged model predicted in Section 4.1, which is of order 10%, and modest compared to the measurement errors. Error bars were calculated to a 90% confidence level.

To better illustrate the improvement achieved by our new model in constraining the physical parameters, we have produced the contour plots for the spin parameter a_* and the inclination angle. In Figure 11 solid lines show the 69%, 90%, and 99% confidence regions of these two parameters for the fit using the angle-resolved (**angleon=1**) option in the new model **relxill**. Dashed-lines show the same contours obtained while fitting with the angle-averaged solution (**angleon=0**). The crosses show the position of the minimum value of χ^2 for each case. Although both fit recover similar best-fit values, the accuracy in the determination of both the spin and inclination is significantly higher with the angle-resolved model. One can see that both parameters are better determined at 90% level with the new model than a 69% level with the old model. With this particular test case we have shown the capabilities of the new model in the interpretation of X-ray spectra from accreting sources, as it constitutes a more consistent and physical description of the reflected spectra from accretion disks around black holes.

Evidently, this is just one particular example of the potential of the new model in

fitting X-ray observations significantly improved: the errors in both spin and inclination are better

7. Summary and Conclusions

The solution of the angular distribution of X-ray reflection from an accretion disk has been calculated with our reflection code XILLVER. The reflected spectrum at any given angle shows clear discrepancies of up to $\sim 25\%$ when compared to the angle-averaged solution. This is observed to occur for all angles, and at any ionization parameter. In particular, scattered continuum photons and line photons respond differently to the angular effects, since the optical depth can be significantly different at different energies. Notably, the Fe K emission line complex becomes weaker for high viewing angles, which agrees with earlier claims of the decrease of the line equivalent width when observed at grazing angles (e.g. Basko 1978; Matt et al. 1992; Martocchia et al. 2000; Reynolds et al. 2004). The angular effects are introduced in the reprocessed radiation mainly by changing the effective optical depth $\tau_{\text{eff}} = \tau/\mu$, where μ is the cosine of the viewing angle. The angular effects are much more extreme at energies where the photoelectric absorption dominates over the Compton scattering. At high energies ($\gtrsim 20$ keV), Compton scattering is the only source of opacity, and thus the angular effects are independent of the ionization of the gas. An important consequence of these effects is that they change the slope of the reflected spectrum as the angular-dependency acts differently at different energies.

The new reflection models predict a limb-brightening law, i.e., the reflected flux integrated over all energies becomes larger at high inclination angles, which agrees well with hydrostatic calculations of Róžańska & Madej (2008) and Róžańska et al. (2011). However, its functional form does not agree with the commonly used law $I \propto \ln(1 + 1/\mu)$ (Haardt 1993), instead, our calculations show a profile less steep. When the atmosphere is

highly ionized ($\log \xi > 3$), the profile becomes even flatter, approaching to the isotropic case. By carrying out calculations of a pure scattering atmosphere, we have shown that this is expected as Compton scattering is essentially isotropic for the reflected spectra of irradiated plane-parallel slabs. In the context of *unblurred reflection*, we expect that these models will be most relevant in analyzing data from astrophysical systems at either very low or very high inclination angles. A new XILLVER table which includes the inclination as a model parameter is provided in the proper format³ for its implementation via the `atable` model in XSPEC.

The table of reflection spectra mentioned above is intended to be used to model an unblurred reflection component, as is the case of the distant cold reflection observed in many AGN. However, it is important to emphasize that when relativistic effects need to be taken into account, a convolution with blurring models in the usual fashion (e.g. `relconv` \times `xillver`) is in fact incorrect, as the proper link of the two models needs to be done intrinsically at each radial zone. Instead, we advise observers to implement the newly developed model `relxill`⁴, which properly integrates the two models. An additional version of this model (`relxill_lp`), in which the illumination is prescribed under a *lampost* scenario, is also provided. The relativistic effects introduce additional directionality dependences in the final reflected spectrum. In general, deviations from the angle-averaged solution can be as large as 20%, and like in the unblurred reflection case, lines and continuum respond in a different way. The main effect is that, at any given inclination, a distant observer will not only see those photons that are emitted into its line of sight, but also those emitted at different directions, but for which the light bending effects are enough to modify their path so that they eventually point toward the observer (for instance, at grazing angles, an

³<http://hea-www.cfa.harvard.edu/~javier/xillver/>

⁴<http://www.sternwarte.uni-erlangen.de/research/relxill/>

observer can even see photons emitted behind the black hole, due to the extreme space-time curvature).

Models calculated in a lampost geometry, where the illumination of the disk is mostly prescribed by the height of the source over the accretion disk, also differ significantly from their angle-averaged counterparts. We found that for either very low or very high inclinations, the discrepancies in the Fe K line band can be as large as 40%. It is worthwhile to mention that all these relative differences are for the reflection spectrum only. In real observations, the observed spectrum is a combination of the reflected and the direct component which illuminates the disk. In many cases the reflection spectrum may only contribute 10 – 20% of the 2 – 10 keV flux of the direct continuum, which dilutes the reflection features and consequently the deviations seen between the new and the old versions of the models. In cases where the height of the illumination source is low ($h \sim 2 - 10 r_g$), the distribution of emission angles that are actually observed at a given inclination becomes very flat. This degree of angular mixing is most pronounced when the disk is observed at high inclination angles. Accordingly, when relativistic effects are extreme, an observer is detecting photons from almost all angles with similar contribution, which essentially acts as an averaging of the reflected spectra over all angles.

We have also carried out a detailed error analysis of the physical parameters derived from fitting these models to simulated data. Our main goal is to show an estimate of the bias introduced by the implementation of the approximate (and commonly used) angle-averaged solution for the reflected spectra. By looking at two distinctive cases, i.e., steep and flat irradiation of the disk, we found that the Fe abundance tends to be over-predicted in almost all cases, but in particular for low inclinations. For a large spin and low ionization, the differences can be as large as a factor of two. This could explain the high abundances usually observed in the spectra of many AGN (see for example, Reynolds & Fabian 1997).

Angular effects also influence the spin determination, although the effect is not dramatic for typical parameters. In particular, for large spin and low ionization the spin recovered from the fits is underestimated at low inclinations ($\theta < 50^\circ$), while for larger inclinations originally low spins ($a_* = 0.0$) are overestimated. The bias on the inclination and height of the primary source is only significant in the case of low spin and large inclination angles, for which both quantities can be underestimated. Oddly, the determination of the inclination angle is mostly unaffected when the spin is large.

We have also included an illustrative example of the application of the new model to real observational data. For this, we analyzed the *Suzaku* spectrum of the Seyfert 1 galaxy Ark 120. The same fit is performed using the angle-averaged solution and the complete angle-dependent model. The differences in the recovered parameters are modest. Nevertheless, the differences in the constrain of the physical parameters is quite significant. The accuracy of the new model in the determination of both the inclination and the spin parameter a_* at a 90% confidence level is superior than the old, angle-averaged model at 69% confidence level. This test case demonstrates the capabilities of the new model, which is more consistent and physical than previous versions. It also illustrates its relevance in the interpretation of observational data from accreting sources, and we expect it will have an even greater impact on analyzing higher quality data from the new generation of observatories such as *NuSTAR* and *Astro-H*.

The models presented here are a new step toward a more physical and self-consistent representation of the X-ray reflection from accretion disks. However, additional sources of systematics that could affect the retrieval of physical parameters (e.g. black hole spin) need still to be further investigated. Although recent studies suggest that for some sources the emission region is compact (e.g. Dauser et al. 2013), the exact geometry of the primary source of X-rays, whether it is a corona or the base of jet, is not very well understood.

The assumptions made on this respect affect the way X-rays illuminate the accretion disk. By providing a lamppost version of our reflection model we are taking the first steps to unveil the geometry of the illuminating source. However, further studies (e.g., timing measurements; see Zoghbi et al. 2010; Kara et al. 2013a,b), are required to accurately determine the illumination profile and the physical origin of the primary source itself. The vertical ionization structure of the disk is treated in detail with the models presented here, however, the same ionization parameter is assumed for all radii. The radial profile of the ionization depends on both the illumination and the gas density profiles. This will be subject of future studies. Other sources of systematics are not directly related to the reflection spectrum. For instance, the presence of a warm absorber in several AGN is known to modify the prediction of the fits depending on how this component is being treated (e.g., MCG-6-30-15, Brenneman & Reynolds 2006). However, observations carried out with the new observatory *NuSTAR* in combination with *XMM-Newton* show that we are currently on the edge of being able to distinguish between blurred reflection and absorption (with NGC 1365 being the best example so far, Risaliti et al. 2013). The improved physical description of the illuminated gas is expected to play a major role to disentangle these components by reducing the uncertainties in the X-ray reflection spectrum.

The calculations presented here were performed in the Odyssey cluster of the Research Computing Facilities of the Harvard University. JG and JEM acknowledge the support of NASA grant NNX11AD08G. JFS was supported by NASA Hubble Fellowship grant HST-HF-51315.01. CSR thanks support from NASA under grant NNX10AE41G.

REFERENCES

- Arnaud, K. A. 1996, in *Astronomical Society of the Pacific Conference Series*, Vol. 101, *Astronomical Data Analysis Software and Systems V*, ed. G. H. Jacoby & J. Barnes, 17
- Bardeen, J. M., Press, W. H., & Teukolsky, S. A. 1972, *ApJ*, 178, 347
- Basko, M. M. 1978, *ApJ*, 223, 268
- Beckwith, K., & Done, C. 2004, *MNRAS*, 352, 353
- Brenneman, L. W., & Reynolds, C. S. 2006, *ApJ*, 652, 1028
- Brenneman, L. W., Risaliti, G., Elvis, M., & Nardini, E. 2013, *MNRAS*, 429, 2662
- Brenneman, L. W., et al. 2011, *ApJ*, 736, 103
- Chandrasekhar, S. 1960, *Radiative transfer* (New York: Dover)
- Chiang, C.-Y., Reis, R. C., Walton, D. J., & Fabian, A. C. 2012, *MNRAS*, 425, 2436
- Cunningham, C. T. 1975, *ApJ*, 202, 788
- Cunningham, J. M., & Bardeen, C. T. 1973, *ApJ*, 183, 237
- Dabrowski, Y., Fabian, A. C., Iwasawa, K., Lasenby, A. N., & Reynolds, C. S. 1997, *MNRAS*, 288, L11
- Dauser, T., Garcia, J., Wilms, J., Böck, M., Brenneman, L. W., Falanga, M., Fukumura, K., & Reynolds, C. S. 2013, *MNRAS*, 430, 1694
- Dauser, T., Wilms, J., Reynolds, C. S., & Brenneman, L. W. 2010, *MNRAS*, 409, 1534
- Dauser, T., et al. 2012, *MNRAS*, 422, 1914

- Dove, J. B., Wilms, J., Maisack, M., & Begelman, M. C. 1997, *ApJ*, 487, 759
- Dovčiak, M., Karas, V., & Yaqoob, T. 2004, *ApJS*, 153, 205
- Duro, R., et al. 2011, *A&A*, 533, L3
- Fabian, A. C., Guilbert, P. W., & Ross, R. R. 1982, *MNRAS*, 199, 1045
- Fabian, A. C., Iwasawa, K., Reynolds, C. S., & Young, A. J. 2000, *PASP*, 112, 1145
- Fabian, A. C., & Vaughan, S. 2003, *MNRAS*, 340, L28
- Fabian, A. C., et al. 2002, *MNRAS*, 335, L1
- Fabian, A. C., et al. 2012a, *MNRAS*, 419, 116
- . 2012b, *MNRAS*, 424, 217
- Feautrier, P. 1964, *Comptes Rendus Academie des Sciences (serie non specifee)*, 258, 3189
- Fukumura, K., & Kazanas, D. 2007, *ApJ*, 664, 14
- Gallo, L. C., Miniutti, G., Miller, J. M., Brenneman, L. W., Fabian, A. C., Guainazzi, M., & Reynolds, C. S. 2011, *MNRAS*, 411, 607
- García, J., Dauser, T., Reynolds, C. S., Kallman, T. R., McClintock, J. E., Wilms, J., & Eikmann, W. 2013, *ApJ*, 768, 146
- García, J., & Kallman, T. R. 2010, *ApJ*, 718, 695
- García, J., Kallman, T. R., & Mushotzky, R. F. 2011, *ApJ*, 731, 131
- George, I. M., & Fabian, A. C. 1991, *MNRAS*, 249, 352
- Ghisellini, G., Haardt, F., & Matt, G. 1994, *MNRAS*, 267, 743

- Haardt, F. 1993, *ApJ*, 413, 680
- Houck, J. C., & Denicola, L. A. 2000, in *Astronomical Society of the Pacific Conference Series*, Vol. 216, *Astronomical Data Analysis Software and Systems IX*, ed. N. Manset, C. Veillet, & D. Crabtree, 591
- Kallman, T., & Bautista, M. 2001, *ApJS*, 133, 221
- Kara, E., Fabian, A. C., Cackett, E. M., Steiner, J. F., Uttley, P., Wilkins, D. R., & Zoghbi, A. 2013a, *MNRAS*, 428, 2795
- Kara, E., Fabian, A. C., Cackett, E. M., Uttley, P., Wilkins, D. R., & Zoghbi, A. 2013b, *MNRAS*, 434, 1129
- Kerr, R. P. 1963, *Phys. Rev. Lett.*, 11, 237
- Laor, A. 1991, *ApJ*, 376, 90
- Lightman, A. P., Lamb, D. Q., & Rybicki, G. B. 1981, *ApJ*, 248, 738
- Lightman, A. P., & Rybicki, G. B. 1980, *ApJ*, 236, 928
- Lightman, A. P., & White, T. R. 1988, *ApJ*, 335, 57
- Magdziarz, P., & Zdziarski, A. A. 1995, *MNRAS*, 273, 837
- Martocchia, A., Karas, V., & Matt, G. 2000, *MNRAS*, 312, 817
- Martocchia, A., & Matt, G. 1996, *MNRAS*, 282, L53
- Matt, G., Fabian, A. C., & Ross, R. R. 1996, *MNRAS*, 278, 1111
- Matt, G., Perola, G. C., & Piro, L. 1991, *A&A*, 247, 25
- Matt, G., Perola, G. C., Piro, L., & Stella, L. 1992, *A&A*, 257, 63

- Miller, J. M., Homan, J., Steeghs, D., Rupen, M., Hunstead, R. W., Wijnands, R., Charles, P. A., & Fabian, A. C. 2006, *ApJ*, 653, 525
- Miller, L., Turner, T. J., & Reeves, J. N. 2008, *A&A*, 483, 437
- Nardini, E., Fabian, A. C., Reis, R. C., & Walton, D. J. 2011, *MNRAS*, 410, 1251
- Niedźwiecki, A., & Życki, P. T. 2008, *MNRAS*, 386, 759
- Patrick, A. R., Reeves, J. N., Porquet, D., Markowitz, A. G., Lobban, A. P., & Terashima, Y. 2011, *MNRAS*, 411, 2353
- Ponti, G., et al. 2010, *MNRAS*, 406, 2591
- Reis, R. C., Fabian, A. C., Ross, R. R., Miniutti, G., Miller, J. M., & Reynolds, C. 2008, *MNRAS*, 387, 1489
- Reynolds, C. S., Brenneman, L. W., Lohfink, A. M., Trippe, M. L., Miller, J. M., Fabian, A. C., & Nowak, M. A. 2012, *ApJ*, 755, 88
- Reynolds, C. S., Brenneman, L. W., Wilms, J., & Kaiser, M. E. 2004, *MNRAS*, 352, 205
- Reynolds, C. S., & Fabian, A. C. 1997, *MNRAS*, 290, L1
- Reynolds, C. S., & Nowak, M. A. 2003, *Phys. Rep.*, 377, 389
- Reynolds, C. S., Nowak, M. A., & Maloney, P. R. 2000, *ApJ*, 540, 143
- Risaliti, G., et al. 2013, *Nature*, 494, 449
- Ross, R. R., & Fabian, A. C. 2005, *MNRAS*, 358, 211
- Róžańska, A., & Madej, J. 2008, *MNRAS*, 386, 1872
- Róžańska, A., Madej, J., Konorski, P., & Sądowski, A. 2011, *A&A*, 527, A47

- Shakura, N. I., & Sunyaev, R. A. 1973, *Å*, 24, 337
- Speith, R., Riffert, H., & Ruder, H. 1995, *Comp. Phys. Commun.*, 88, 109
- Steiner, J. F., et al. 2011, *MNRAS*, 416, 941
- Svoboda, J., Dovčiak, M., Goosmann, R., & Karas, V. 2009, *A&A*, 507, 1
- Vrtilek, S. D., Soker, N., & Raymond, J. C. 1993, *ApJ*, 404, 696
- Walton, D. J., Nardini, E., Fabian, A. C., Gallo, L. C., & Reis, R. C. 2013, *MNRAS*, 428, 2901
- Wilkins, D. R., & Fabian, A. C. 2011, *MNRAS*, 414, 1269
- . 2012, *MNRAS*, 424, 1284
- Wilms, J., Reynolds, C. S., Begelman, M. C., Reeves, J., Molendi, S., Staubert, R., & Kendziorra, E. 2001, *MNRAS*, 328, L27
- Zoghbi, A., Fabian, A. C., Uttley, P., Miniutti, G., Gallo, L. C., Reynolds, C. S., Miller, J. M., & Ponti, G. 2010, *MNRAS*, 401, 2419

Table 1: Fractional bias of the parameters spin, iron abundance and height when using the angle-averaged approximation for the reflected radiation. The difference between the original value and the one recovered after the fit is shown for each parameter. All uncertainties are given at 90% confidence.

			— $\log \xi = 0.0$ —				— $\log \xi = 3.0$ —			
	a_*	h	$\theta = 20^\circ$	$\theta = 40^\circ$	$\theta = 60^\circ$	$\theta = 80^\circ$	$\theta = 20^\circ$	$\theta = 40^\circ$	$\theta = 60^\circ$	$\theta = 80^\circ$
A_{Fe}	0.99	3	1.14 ± 0.07	$1.00^{+0.15}_{-0.09}$	0.42 ± 0.07	0.02 ± 0.03	$0.57^{+0.09}_{-0.12}$	$0.44^{+0.10}_{-0.09}$	0.27 ± 0.11	$-0.00^{+0.10}_{-0.02}$
a_*	0.99	3	0.00 ± 0.01	$-0.00^{+0.01}_{-0.02}$	$0.01^{+0.00}_{-0.01}$	$0.01^{+0.00}_{-0.01}$	$-0.12^{+0.05}_{-0.04}$	$-0.12^{+0.06}_{-0.05}$	-0.02 ± 0.02	$-0.00^{+0.01}_{-0.27}$
θ	0.99	3	$1.97^{+0.69}_{-0.67}$	$0.44^{+0.31}_{-0.36}$	$-0.39^{+0.18}_{-0.20}$	$-0.23^{+0.20}_{-0.16}$	$-1.92^{+1.51}_{-1.00}$	$-2.03^{+1.08}_{-1.16}$	$-0.09^{+0.43}_{-0.48}$	$0.00^{+0.00}_{-1.86}$
A_{Fe}	0.00	3	0.21 ± 0.02	$0.18^{+0.02}_{-0.03}$	0.09 ± 0.02	-0.16 ± 0.03	0.16 ± 0.04	0.13 ± 0.04	0.08 ± 0.05	$0.07^{+0.11}_{-0.09}$
a_*	0.00	3	$-0.06^{+0.04}_{-0.03}$	$-0.06^{+0.08}_{-0.05}$	$-0.05^{+0.09}_{-0.06}$	$0.13^{+0.17}_{-0.36}$	$-0.00^{+0.12}_{-0.07}$	$-0.07^{+0.17}_{-0.15}$	$0.56^{+0.20}_{-0.57}$	$0.97^{+0.03}_{-1.09}$
θ	0.00	3	$0.09^{+0.31}_{-0.39}$	$-0.04^{+0.14}_{-0.20}$	$0.27^{+0.20}_{-0.19}$	$-4.79^{+4.16}_{-1.13}$	$-0.34^{+1.30}_{-1.34}$	$0.11^{+0.49}_{-0.59}$	$0.81^{+0.91}_{-1.06}$	$-4.91^{+1.03}_{-2.20}$
A_{Fe}	0.99	50	0.25 ± 0.02	0.14 ± 0.02	-0.03 ± 0.03	$-0.07^{+0.03}_{-0.02}$	0.16 ± 0.03	0.12 ± 0.03	$-0.00^{+0.08}_{-0.01}$	-0.06 ± 0.03
a_*	0.99	50	$-1.99^{+0.37}_{-0.01}$	$-1.99^{+1.01}_{-0.00}$	$0.01^{+0.00}_{-1.76}$	$0.01^{+0.00}_{-0.03}$	$-1.99^{+2.00}_{-0.01}$	$-1.98^{+1.99}_{-0.01}$	$0.01^{+0.00}_{-2.00}$	$0.00^{+0.01}_{-2.00}$
θ	0.99	50	0.29 ± 0.20	$-0.07^{+0.44}_{-0.42}$	$0.43^{+2.95}_{-1.99}$	$-21.22^{+1.60}_{-1.23}$	$0.62^{+0.79}_{-0.82}$	$-0.06^{+1.81}_{-1.33}$	$0.80^{+4.90}_{-3.74}$	$-12.55^{+12.55}_{-5.09}$
A_{Fe}	0.00	50	0.27 ± 0.02	0.15 ± 0.02	-0.03 ± 0.03	$-0.08^{+0.03}_{-0.02}$	0.17 ± 0.03	0.12 ± 0.03	$0.00^{+0.07}_{-0.02}$	-0.07 ± 0.03
a_*	0.00	50	$-1.00^{+0.49}_{-0.00}$	$-1.00^{+0.90}_{-0.00}$	$1.00^{+0.01}_{-1.55}$	$1.00^{+0.00}_{-0.04}$	$-1.00^{+2.00}_{-0.00}$	$-1.00^{+2.00}_{-0.01}$	$0.77^{+0.23}_{-1.78}$	$0.99^{+0.01}_{-1.99}$
θ	0.00	50	0.25 ± 0.20	$0.10^{+0.46}_{-0.41}$	$-0.86^{+1.95}_{-1.78}$	$-22.10^{+2.19}_{-0.86}$	$0.72^{+0.80}_{-0.82}$	$0.03^{+1.84}_{-1.35}$	$1.20^{+5.80}_{-3.65}$	$-16.09^{+5.17}_{-3.49}$

Table 2. Best-fit parameters for Ark 120 data

Component	Parameter	Value	Value
relxill	$q_{in} = q_{out}$	$4.4^{+2.0}_{-1.2}$	$4.8^{+1.8}_{-1.1}$
relxill	a	$0.674^{+0.118}_{-0.203}$	$0.655^{+0.122}_{-0.126}$
relxill	i (deg)	$45.0^{+5.3}_{-2.7}$	$45.3^{+4.8}_{-2.4}$
relxill	R_{in} (ISCO)	1	1
relxill	R_{out} (ISCO)	400	400
relxill	z	0.0327	0.0327
relxill	Γ	$2.17^{+0.02}_{-0.01}$	$2.17^{+0.02}_{-0.01}$
relxill	$\log \xi$	$1.03^{+0.16}_{-0.26}$	$0.84^{+0.24}_{-0.10}$
relxill	A_{Fe}	$1.54^{+0.44}_{-0.45}$	$1.78^{+0.39}_{-0.40}$
relxill	angleon	0	1
relxill	$N(10^{-4})$	$1.81^{+0.32}_{-0.29}$	$2.07_{-0.2}$
xillver	$N(10^{-4})$	$1.55^{+0.42}_{-0.40}$	$0.14^{+0.07}_{-0.04}$

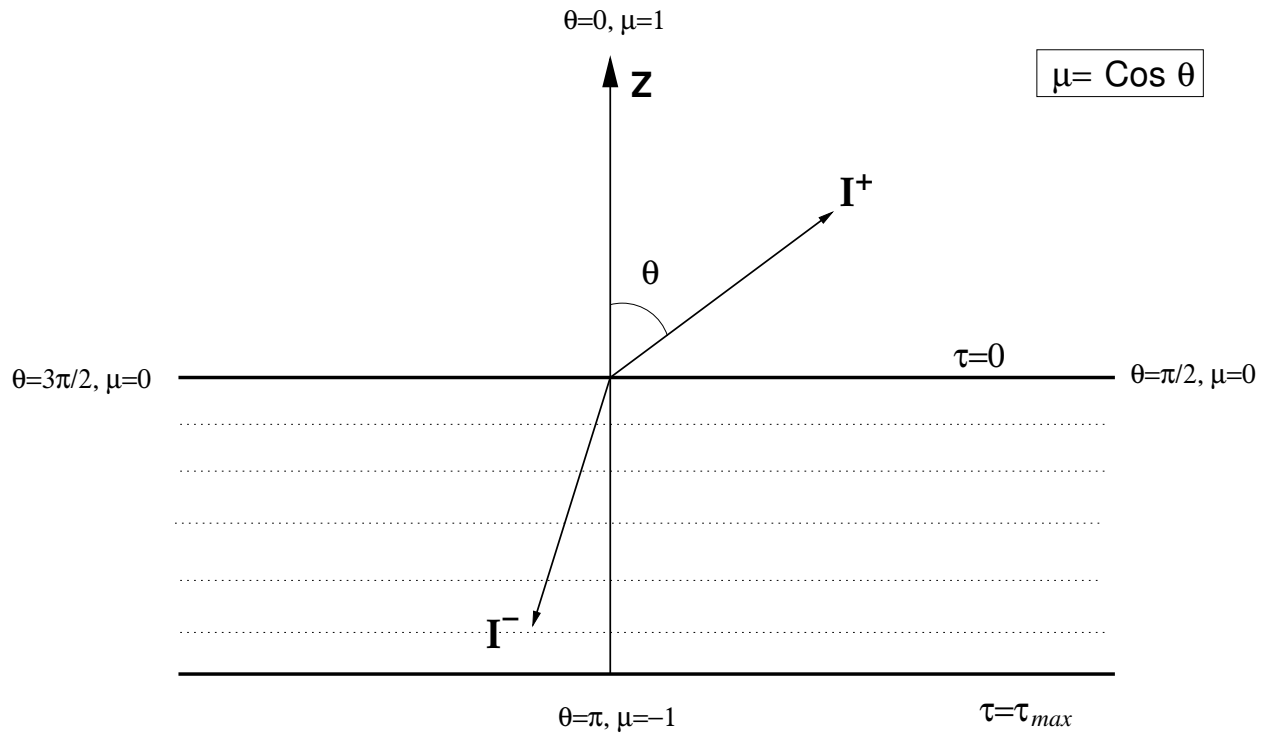


Fig. 1.— Plane-parallel slab with the incoming and outgoing radiation fields.

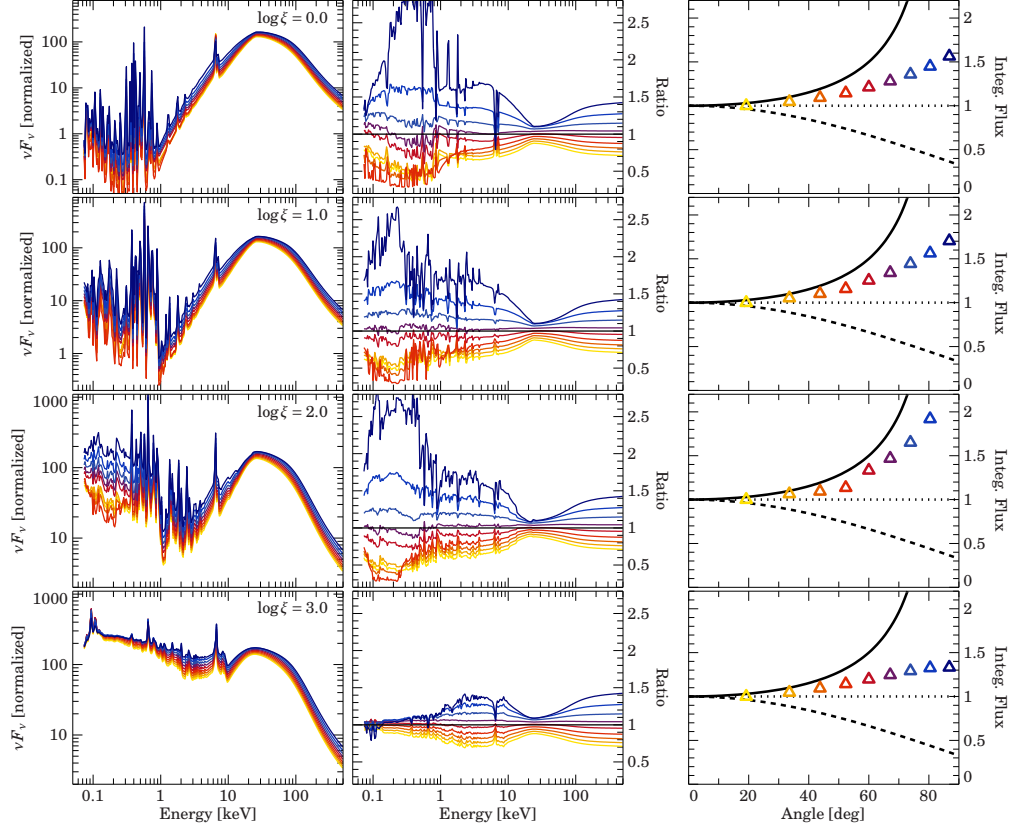


Fig. 2.— Left panels: Angular distribution of the reflected spectrum from an accretion disk calculated with XILLVER. Middle panels: ratio of the angular solution to the angle-average. Right panels: Integrated flux as a function of the viewing angle. Each angular solution is identified with a different color. Each row of panels correspond to a particular ionization parameter, as indicated in the left panels. The solid and dashed lines represent the limb-brightening ($I \propto \ln(1+1/\mu)$ Haardt 1993) and darkening laws ($I \propto \ln(1+2.06\mu)$ Laor 1991), respectively, which are commonly used in relativistic blurring kernels.

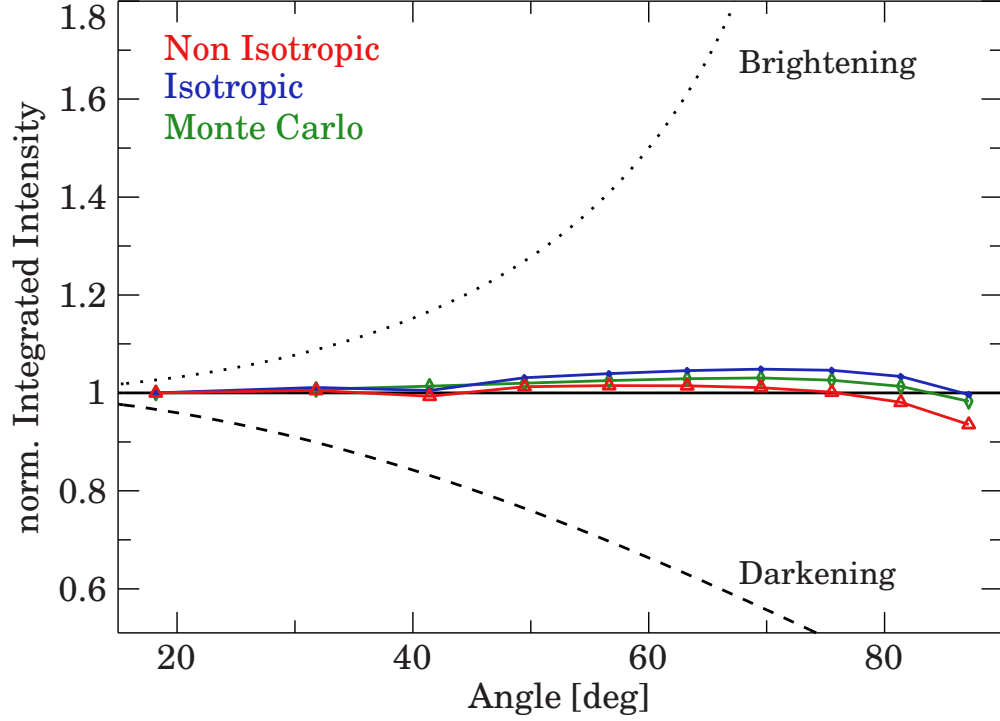


Fig. 3.— Angular-dependence of the integrated flux emergent from an irradiated accretion disk. The limb-brightening and darkening laws are shown in green and gray for reference (see Figure 2). A pure scattering XILLVER calculation is shown in blue (circles), which follows an isotropic profile. A similar calculation (in red, triangles) that includes a phase function in the radiative transfer calculation shows a very similar profile. The flatness is understood to reflect the intrinsic angle averaging which occurs due to many scatterings (i.e., the original emission angle information is lost). This result is confirmed with a Monte Carlo simulation under the same conditions, shown in green (diamonds).

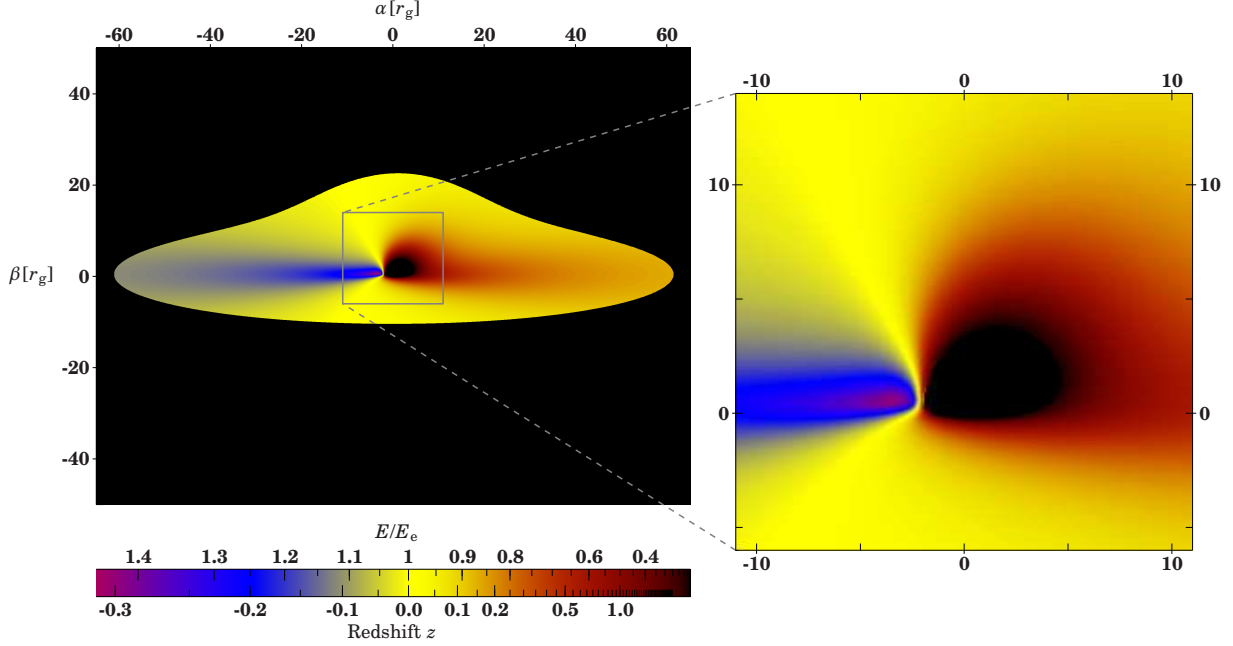


Fig. 4.— Map of an accretion disk around a maximally spinning black hole ($a = 0.998$) as seen by a distant observer at an inclination angle of $\theta = 80^\circ$. The disk ranges from the marginally stable radius ($r_{\text{in}} = 1.24 r_g$) to $r_{\text{out}} = 60 r_g$. α and β are the coordinates defined on the plane of the sky (i.e., perpendicular to the line of sight; see Cunningham & Bardeen 1973, equation 28). The color scale shows the energy shift of the photons; the geometric asymmetries are due to relativistic light bending. The blue-shifted (left) part of the disk moves towards the observer, whereas the right part recedes from the observer.

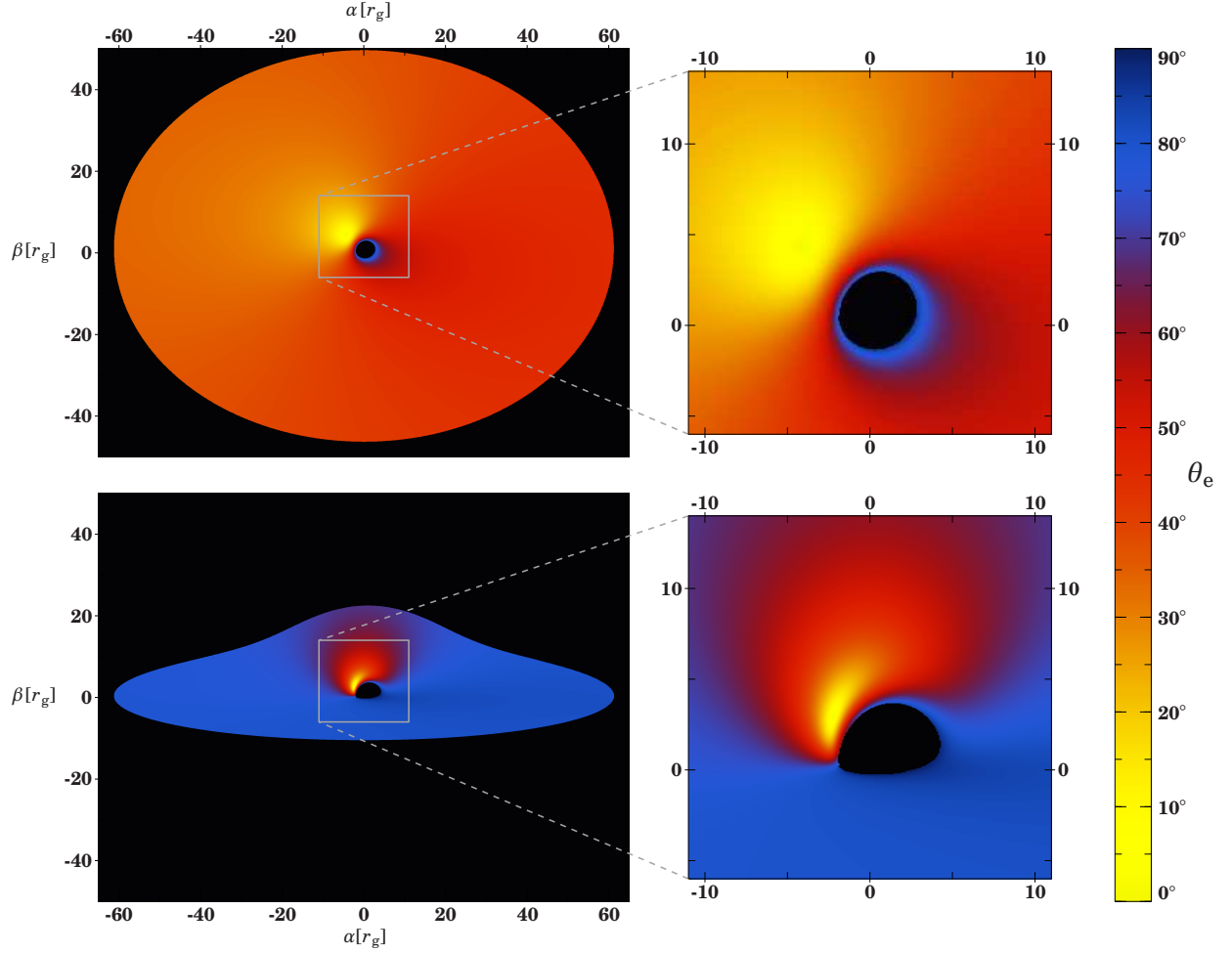


Fig. 5.— Map of an accretion disk similar to Figure 4, except that now the emission angle θ_e is depicted by the color scaling on the accretion disk. The disk is displayed for angles of $\theta = 40^\circ$ (upper panel) and $\theta = 80^\circ$ (lower panel). While θ_e takes almost any value close to the black hole, it is apparent that for increasing distance to the black hole this angle converges towards the inclination of the system.

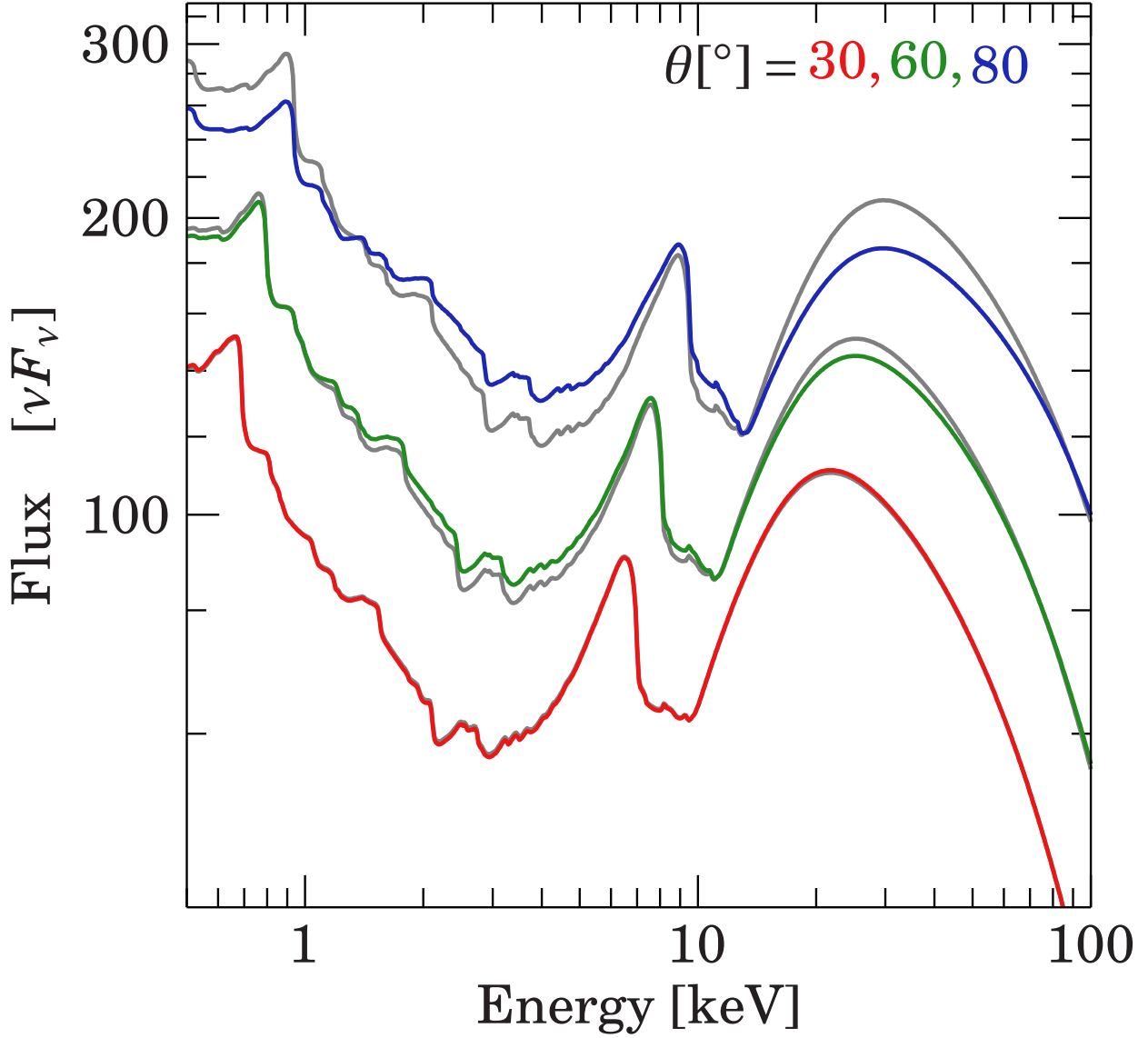


Fig. 6.— Reflected spectrum calculated self-consistently with the new model `relxill` for different inclination angles. For each case, the prediction obtained with simple convolution of `relconv` on the angle-dependent `xillver` spectra (with angles linked) is shown in grey, demonstrating the importance of the correct implementation of the angular solutions. Differences are bigger for larger inclinations because the relativistic effects are stronger. The other parameters are common to all spectra, i.e., ionization parameter $\log \xi = 3$, photon index $\Gamma = 2$, emissivity $q = 3$, and spin parameter $a_* = 0.998$.

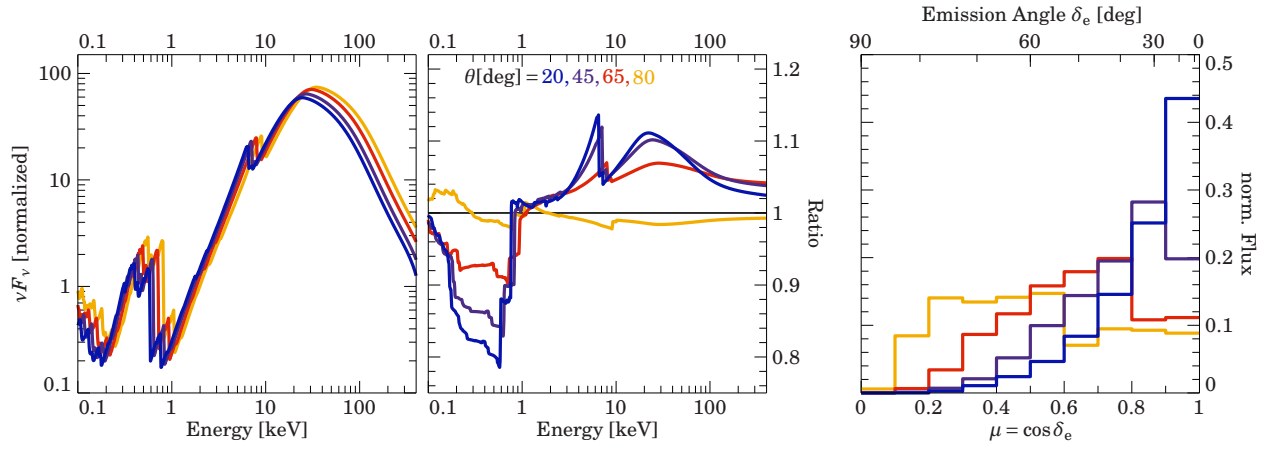


Fig. 7.— Left panel: The **relxill** model for a typical parameter combination (ionization parameter $\xi = 1$, photon index $\Gamma = 2$, and the standard emissivity $I \propto r^{-3}$) for different inclinations. Middle panel: The ratio between **relxill** and the usual convolution of **xillver** with **relconv**. Right panel: Distribution of the flux across the range of emission angles. Note that a normal reflection code would assume a constant distribution here.

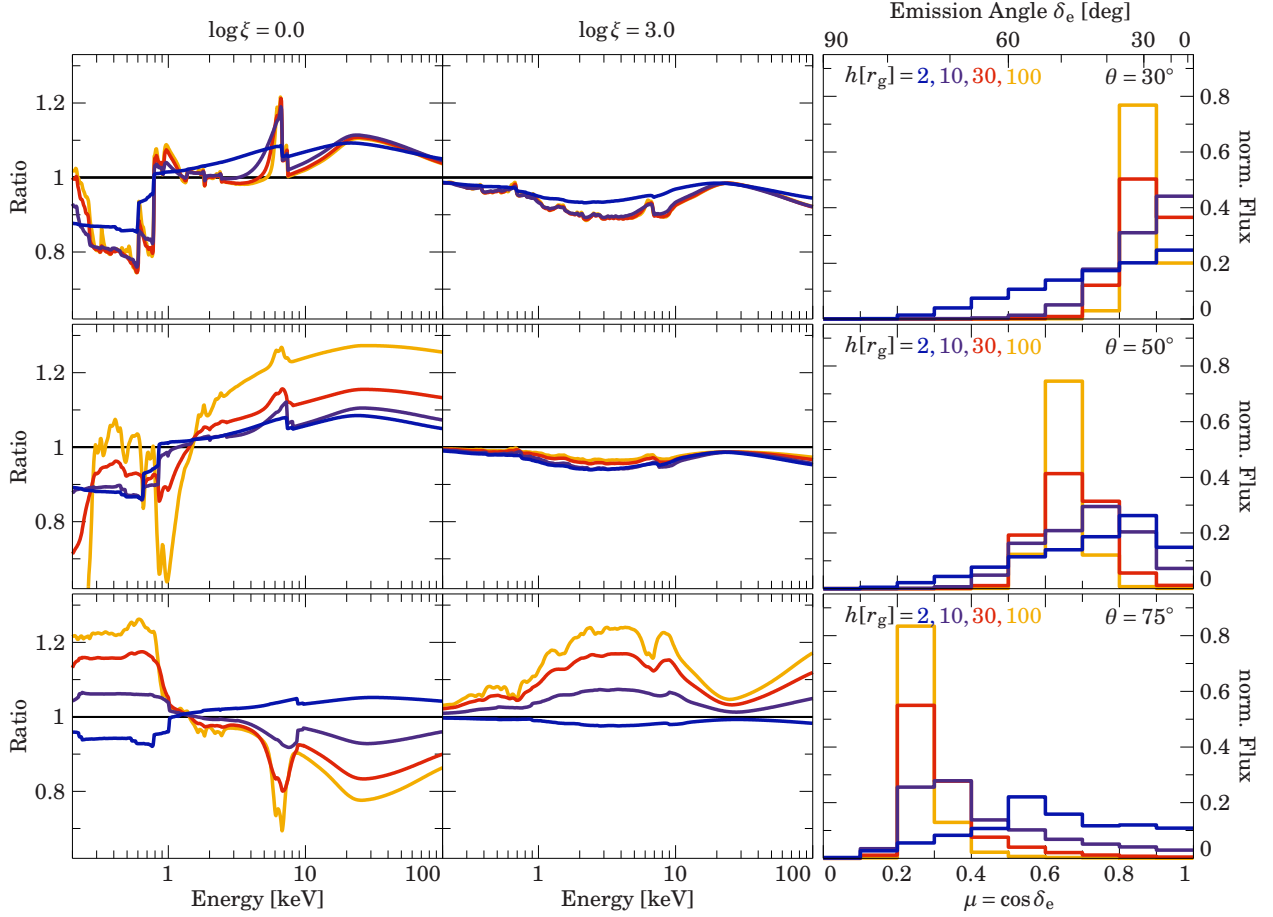


Fig. 8.— The `relxill_lp` model, which predicts the relativistically blurred reflected spectrum in a lampost geometry for a combination of typical parameters. Left and middle panels show the ratio of the new model to the angle-averaged solution for $\log \xi = 0$ and 3, respectively, while the right panel shows the distribution of emission angles at which photons are emitted out of the accretion disk. Top, middle, and bottom panels correspond to inclination (viewing) angles $\theta = 30^\circ, 50^\circ$ and 75° , respectively. Different colors indicate the height of the primary source, as shown in the right panels.

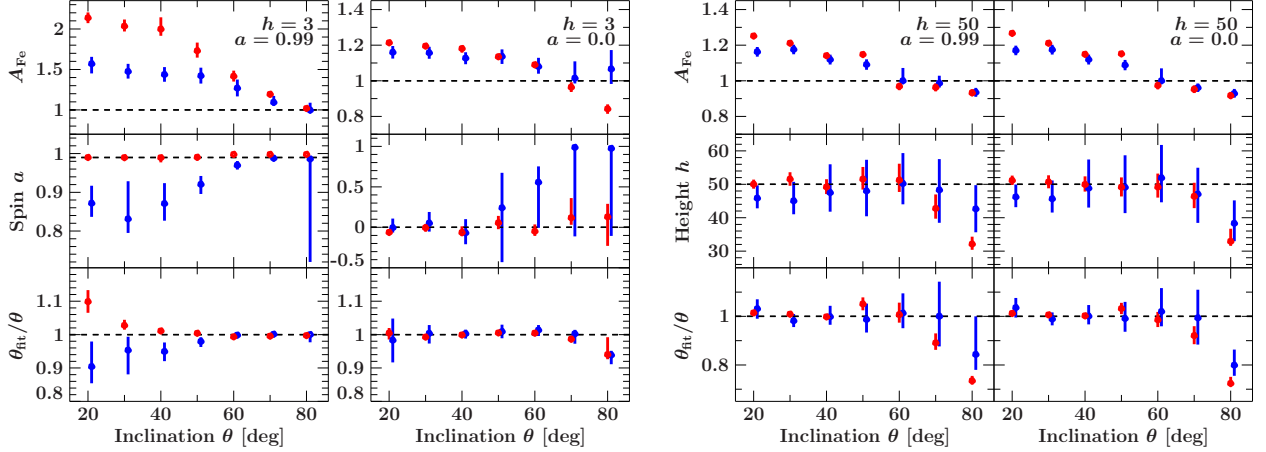


Fig. 9.— Results from simulating a 100 ksec *XMM-Newton* observation of an unblurred reflection spectrum assuming the angle-dependent model of `relxill_lp`. We have normalized the flux to be commensurate with MCG–6-30-15 (i.e., $3.7 \cdot 10^{-11} \text{ erg s}^{-1} \text{ cm}^{-2}$). Upon being generated with appropriate noise, the data are fitted using the angle averaged model `relconv_lp` \times `xillver`. The input ionization of the accretion disk is chosen to be $\xi = 1$ (red, low ionization) or $\xi = 10^3$ (blue, high ionization). We choose standard initial values of the photon index ($\Gamma = 2$) and iron abundance ($A_{\text{Fe}} = 1$). All combinations are simulated for different input inclinations, while we allow all fit parameters (the normalization, ξ , a , θ , A_{Fe} , and h) to vary freely. In the bottom panels, we show how the fitted inclination deviates from the input value. **Left:** Results for a low source height ($h = 3 r_g$), which produces strongly concentrated irradiation in the innermost parts of the accretion disk. **Right:** A larger source height ($h = 50 r_g$), which more strongly illuminates the outer disk. The spin cannot be well constrained for such a large height (see Dauser et al. 2013), so we plot the deviation in height h rather than spin.

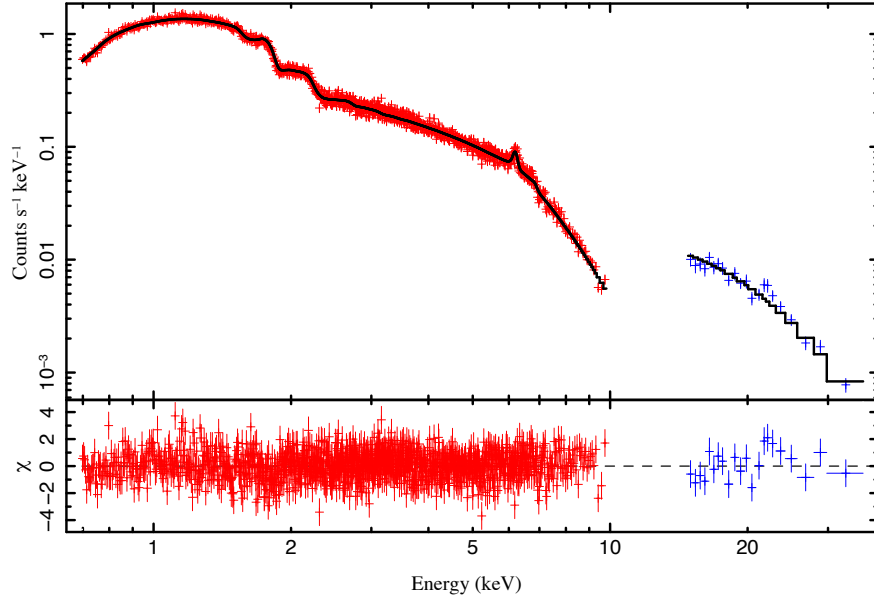


Fig. 10.— *Suzaku* spectrum of the Seyfert 1 galaxy Ark 120. Data points in red show the front-illuminated co added XIS CCD data in the 0.7-10 keV band. Blue data points show the PIN data covering the 15-45 keV range. The solid black line is the best fit using the new `relxill` model (with `angleon=1`). Residuals are shown in the lower panel. Error bars are calculated to a 90% confidence level.

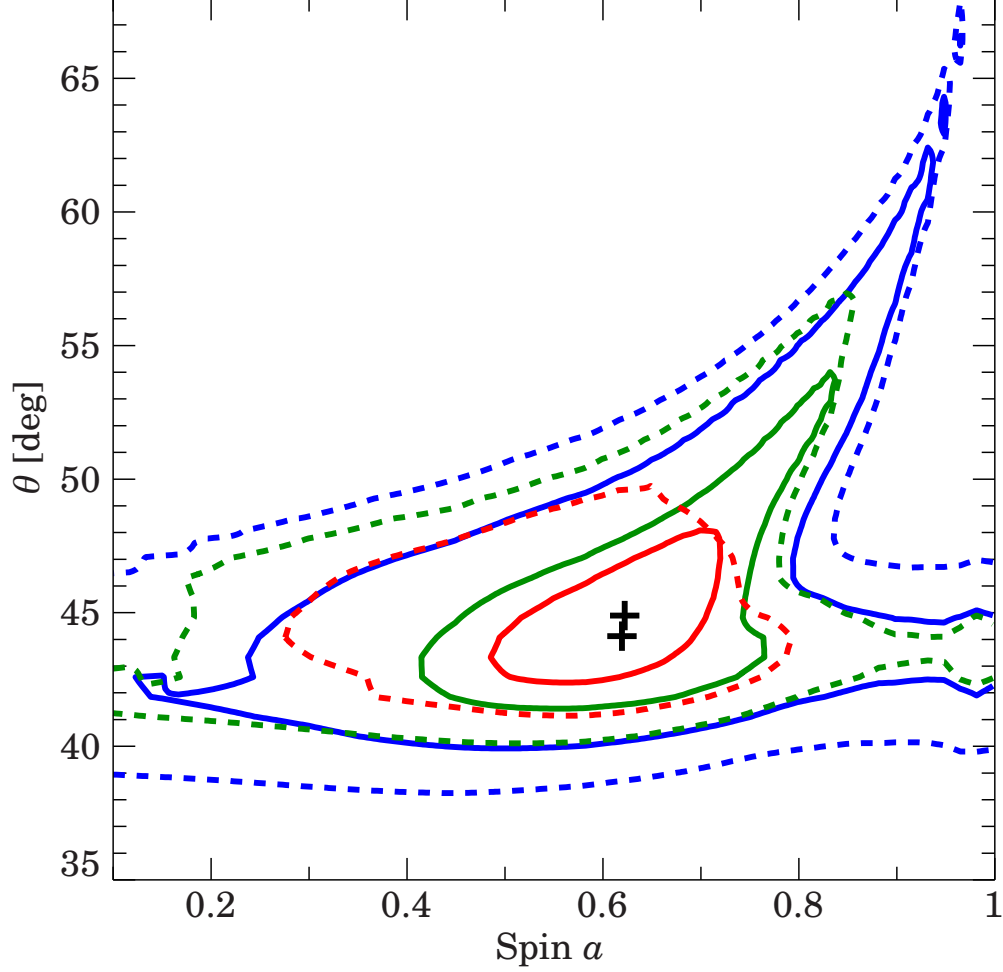


Fig. 11.— Contour plots of the inclination and spin parameter a_* for the fits to the *Suzaku* spectrum of Ark 120. Red, green, and blue solid lines represent the 69%, 90%, and 99% confidence regions for the `relxill` fit with `angleon=1`, respectively. The dashed-lines show the same regions (in the same order) for the fit with `angleon=0` (angle-averaged solution). The black crosses show the position of the minimum χ^2 for each fit, which indicates the best-fit parameters. The model parameters are constrained significantly better when the new version of the model is implemented.